



Engineering of Z-scheme 2D/3D architectures with Ni(OH)_2 on 3D porous $\text{g-C}_3\text{N}_4$ for efficiently photocatalytic H_2 evolution

Ruya Cao, Hongcen Yang, Shouwei Zhang*, Xijin Xu*

School of Physics and Technology, University of Jinan, 336 West Road of Nan Xin zhuang, Jinan, 250022, Shandong, PR China



ARTICLE INFO

Keywords:

Z-scheme
2D Ni(OH)_2 nanosheets
3D $\text{g-C}_3\text{N}_4$
Electrostatic self-assembly

ABSTRACT

The construction of Z-scheme system to achieve efficient photolysis of water to produce hydrogen is a promising approach in the field of photocatalysis. In this work, two dimensionally (2D) crystallized Ni(OH)_2 nanosheets are loaded upon the surfaces of three dimensionally macroporous $\text{g-C}_3\text{N}_4$ (3D $\text{g-C}_3\text{N}_4$) via the electrostatic method, synthesizing 2D/3D $\text{Ni(OH)}_2/\text{g-C}_3\text{N}_4$ (Ni/DOMCN) Z-scheme system. The optimized photocatalysts exhibit apparent quantum efficiency (AQE) of 8.2% at 400 nm and an excellent H_2 -production rate of $\sim 87.2 \mu\text{mol h}^{-1}$ under visible light ($\lambda > 400 \text{ nm}$), which is ~ 76 times higher than unmodified 3D $\text{g-C}_3\text{N}_4$. The excellent cyclic performance of optimized photocatalyst can be attributed to the redox process between $\text{Ni}^{2+}/\text{Ni}^0/\text{NiO}$ during the photocatalytic reaction. The advantages of modified photocatalysts are attributed to the following aspects: (1) The Z-scheme system, accelerating the separation of photogenerated electron-hole pairs and leading to more efficient photocatalytic hydrogen production; (2) 2D/3D hollow structures, facilitating the diffusion of the solution and the light reflections; (3) tight contact, promoting the transfer and separation of photogenerated charge carrier; (4) larger surface area, providing more reactive sites. This work highlights the critical role of the Z-scheme system in solar photolysis and provides new insights into the development of 2D/3D photocatalysts.

1. Introduction

With the more serious energy shortages and environmental contaminations more seriously, searching a clean renewable energy source is become becoming a topmost priority [1,2]. H_2 is considered as the ideal clean energy sources in the 21 st century, which can be produced by photolytic water release and used as a substitute for traditional energy sources such as petroleum [3]. Presently, a large number of photocatalysts used for hydrogen evolution have been reported and studied [4]. Graphite carbon nitride ($\text{g-C}_3\text{N}_4$) composed of carbon along with nitrogen is one of suitable candidate photocatalysts due to its low cost and readily available advantages [5,6]. However, the inherent disadvantages of the $\text{g-C}_3\text{N}_4$ severe limit its photocatalytic performance, such as low photo-generated charge separation efficiency, ease of recombination and lack of surface activity, etc [7,8]. Therefore, many ploys have been exploited to raise the photocatalytic activity of $\text{g-C}_3\text{N}_4$, such as designing nanoporous structures [9], doping elements [10], co-catalyst introduction [11] and constructing heterojunctions [12,13].

The microstructure of a material is tightly related to its properties, then designing 3D ordered nanoporous structures has become a useful method to realize effective separation and extended absorption spectra of photo-generated charges [14–16]. Compared with bulk or sheet-like

structures, 3D ordered macroporous structures have obtained extensive attention in the domain of photocatalysis due to their property slow photon effect, which can delay and store incident light of a specific wavelength in 3D materials, and enhance their light absorption efficiency [7,8,17]. We have designed a 3D $\text{g-C}_3\text{N}_4$ photocatalyst in our previous work, which exhibits a significantly improved photocatalytic property for hydrolyzed hydrogen evolution contrasted to the original bulk $\text{g-C}_3\text{N}_4$ photocatalyst, but the noble metal was still required as a co-catalyst [18–20]. Therefore, it is necessary to modify 3D $\text{g-C}_3\text{N}_4$ to promote photocatalytic activity and reduce production costs.

As we all know, the Z-scheme systems possess the higher charge separation efficiency and stronger redox ability, all of which contribute to photocatalytic activity. Based on these advantages, various Z-scheme photocatalytic systems have been extensively employed to improve the properties of photocatalysts, such as $\text{TiO}_2\text{-Au-CdS}$ [21], $\text{BiVO}_4\text{/Au@CdS}$ [22] and $\text{g-C}_3\text{N}_4\text{/FeWO}_4$ [23].

Nickel-based catalysts have been reported to possess excellent photocatalytic properties. In comparison with the reported Ni-containing species, 2D Ni(OH)_2 nanosheets have a greater solubility product constant because it is capable of releasing more free Ni^{2+} in aqueous solution [24]. The free Ni^{2+} in aqueous solution can be reduced to Ni^0 by the photogenerated electrons. The Ni^0 are unstable in

* Corresponding authors.

E-mail addresses: sps_zhangsw@ujn.edu.cn (S. Zhang), sps_xuxj@ujn.edu.cn (X. Xu).

air, which can be easily oxidized to be NiO. The progress of the photocatalytic hydrogen evolution reaction could be promoted by the redox reaction of $\text{Ni}^{2+}/\text{Ni}^0/\text{NiO}$ [25].

Therefore, the 2D $\text{Ni}(\text{OH})_2$ nanosheets was well complexed with 3D $\text{g-C}_3\text{N}_4$ through heterojunction interface engineering and obtained the 2D $\text{Ni}(\text{OH})_2/3\text{D g-C}_3\text{N}_4$ (3D/2D Ni/DOMCN) Z-scheme system. The electrons located in CB of 3D $\text{g-C}_3\text{N}_4$ will combine with the holes in VB of $\text{Ni}(\text{OH})_2$ along the Z-scheme pathway, thus maintaining the strong electron reducibility in $\text{Ni}(\text{OH})_2$ conduction band (CB) and the strong holes oxidizability in 3D $\text{g-C}_3\text{N}_4$ valence band (VB). There are many common methods to prepare Z-scheme system photocatalysts including hydrothermal [26] and electrostatic self-assembly [27], etc. Among them, electrostatic self-assembly is a simpler, versatile and inexpensive method for easily assembling oppositely charged substances [20].

Here in this work, a novel 2D/3D Z-scheme photocatalyst has been successfully prepared by loading positively charged 2D $\text{Ni}(\text{OH})_2$ nanosheets on the negatively charged 3D $\text{g-C}_3\text{N}_4$ by an ordinary electrostatic method, which makes the preparation method of the material more simple and efficient [28]. The photocatalytic efficiency of as-obtained Ni/DOMCN realizes 76 times higher compared with pure 3D $\text{g-C}_3\text{N}_4$ in visible-light H_2 evolution. Under the same experimental conditions, the activity of photocatalytic H_2 -production for Ni/DOMCN photocatalyst is more excellent by contrast to the Pt/ $\text{g-C}_3\text{N}_4$ photocatalyst, and it has also been indicated that $\text{Ni}(\text{OH})_2$ nanosheets are more effective than other Ni materials based on $\text{g-C}_3\text{N}_4$, indicating that the Z-scheme system not only has the potential to replace noble metals, but also greatly enhances photocatalytic hydrogen evolution performance. Through a detailed analysis of the reaction mechanism, including light absorption, fluorescence and luminescence decay, we have a deep understanding of the factors affecting photocatalytic performance. This work provides new insights into the development of highly active, inexpensive, non-precious metal photocatalysts and the construction of Z-scheme heterojunctions with satisfactory performance.

2. Experimental sections

2.1. Preparation of 3D $\text{g-C}_3\text{N}_4$

The preparation method of SiO_2 was given in previous works [17]. Two solutions were rapidly mixed at a rate of 300 rpm and stirring for 4 h: one solution contained ethanol (90 mL) and tetraethoxysilane (TEOS, 16.8 mL), while another contained water (78 mL), ethanol (84 mL) and ammonium hydroxide ($\text{NH}_3\text{H}_2\text{O}$, 28 wt.%, 30 mL). The SiO_2 with a diameter of 400 nm was obtained by washing and drying. First, the SiO_2 and dicyandiamide with a mass ratio of 1:2 were uniformly dispersed into 100 mL deionized water by ultrasonic waves, and then heated and stirred for 12 h on magnetic heating stirrer under 70 °C. The white powder obtained was put into a covered crucible and calcined at 550 °C for 4 h in a muffle furnace with the heating rate of 2.5 °C/min. The obtained pale yellow sample was ground into a powder and stirred for 12 h in an hydrofluoric acid (HF, 10 wt.%) solution (1 M), and the 3D $\text{g-C}_3\text{N}_4$ sample was obtained by washing and drying.

2.2. Preparation of Ni/DOMCN

1 mmol of nickel chloride hexahydrate ($\text{NiCl}_2\cdot6\text{H}_2\text{O}$, 99.0%) and 3 mmol of ammonium bicarbonate (NH_4HCO_3 , 21.0~22.0%) were added to ethanol (40 mL) and churned for 8 h. The $\text{Ni}(\text{OH})_2$ was then obtained by washing and drying. Subsequently, 3D $\text{g-C}_3\text{N}_4$ (150 mg) was well-dispersed into deionized water (100 mL). 15, 20, 25, 30 and 35 mL of an aqueous solutions of $\text{Ni}(\text{OH})_2$ were added to the above mixture drop by drop and the Ni/DOMCN was obtained by stirring for 3 h. The samples obtained were defined as 15-Ni/DOMCN, 20-Ni/DOMCN, 25-Ni/DOMCN, 30-Ni/DOMCN, 35-Ni/DOMCN, respectively.

2.3. Characterization

The components were surveyed using a Bruker D8 X-ray powder diffractometer (XRD). Fourier transform infrared (FTIR) spectra were measured by Avatar 370, Thermo Nicolet spectrometer. The ultraviolet-visible (UV-vis) diffuse reflectance spectra (DRS) were measured by a UV-vis spectrophotometer (Shimadzu UV-2500) using BaSO_4 as a reference. The thermal behavior of the sample (Model 2050, Beijing Optical Products Co., Ltd.) was determined by thermogravimetric (TG) analysis. Nitrogen adsorption-desorption was performed using the Micromeritics Model ASAP 2020 instrument. The morphologies were measured via transmission electron microscopy (TEM, JEOL JEM-2100F). The chemical component was determined via X-ray photoelectron spectroscopy (XPS, ESCALAB 250). Photoluminescence (PL) and fluorescence decay spectra were measured at room temperature using Fluoromax-4Ctspc. Transient photocurrent-time (I-t) response testing and electrochemical impedance spectroscopy (EIS) testing were carried out by CHI 660E, wherein the bias voltage and the light source were 0.1 V and 50 mW. The electrolyte was the 1.0 M Na_2SO_4 aqueous solution.

2.4. Photocatalytic experiments

The photocatalytic hydrogen evolution experiment was conducted in a glass gas sensor equipment (Beijing Aulight Co., Ltd.) using a 300 W xenon lamp act a visible light source. The Ni/DOMCN catalyst (20 mg) and sacrificial triethanolamine (TEOA, 20 mL) were put into aqueous solution (80 mL), ultrasonically stirred uniformly, and the solution was evacuated and purged with N_2 gas for 30 min to remove air. The closed reactor was kept at 40 ± 0.5 °C among the experiment. The H_2 evolution rates on the 25-Ni/DOMCN was measured by different bandpass filters (365, 380, 400, 420, 450, 475, 500 and 520 nm), where the light intensities were 2.86, 7.14, 9.84, 20.07, 21.62, 19.87, 19.77 and 19.83 mW cm^{-2} , respectively. The apparent quantum yield (AQE) of the material was calculated via the following formula [6,29]. Taking the bandpass filter as 400 nm as an example, the AQE calculation method is as follows:

$$\text{AQE} [\%]$$

$$\begin{aligned} &= \frac{\text{number of reacted electrons}}{\text{number of incident photons}} \times 100 \\ &= \frac{\text{number of evolved hydrogen molecules} \times 2}{\text{number of incident photons}} \times 100 \\ &= \frac{2 \times N_{\text{H}_2}}{N_i} \times 100 \\ &= \frac{2 \times N_{\text{H}_2}}{\frac{I \times A \times \Delta \lambda}{h \times c}} \times 100 \end{aligned}$$

N (number of electrons, photons or molecules), I (light intensity (9.84 mW/cm²)), A (irradiation area (23.7 cm² (r = 2.75 cm))), t (time (3600 s)), λ (wavelength (400 nm)), h (6.02 \times 10⁻³⁴ Js) and c (3.0 \times 10⁸ m/s).

3. Results and discussion

3.1. Structure and characterization

Our synthetic procedure is illustrated in Fig. 1(a). By testing the zeta potential of the material, the 3D $\text{g-C}_3\text{N}_4$ is found to possess the negative charge at pH < 9 and the positive charge at pH > 9, while the $\text{Ni}(\text{OH})_2$ nanosheets are opposite. Therefore, 2D $\text{Ni}(\text{OH})_2$ nanosheets can be attached to the 3D $\text{g-C}_3\text{N}_4$ surface uniformly on account of the electrostatic attraction in the pH range of ~5–12. Further, Fig. 1(b) shows the precipitations by mixing 3D $\text{g-C}_3\text{N}_4$ and $\text{Ni}(\text{OH})_2$ nanosheets

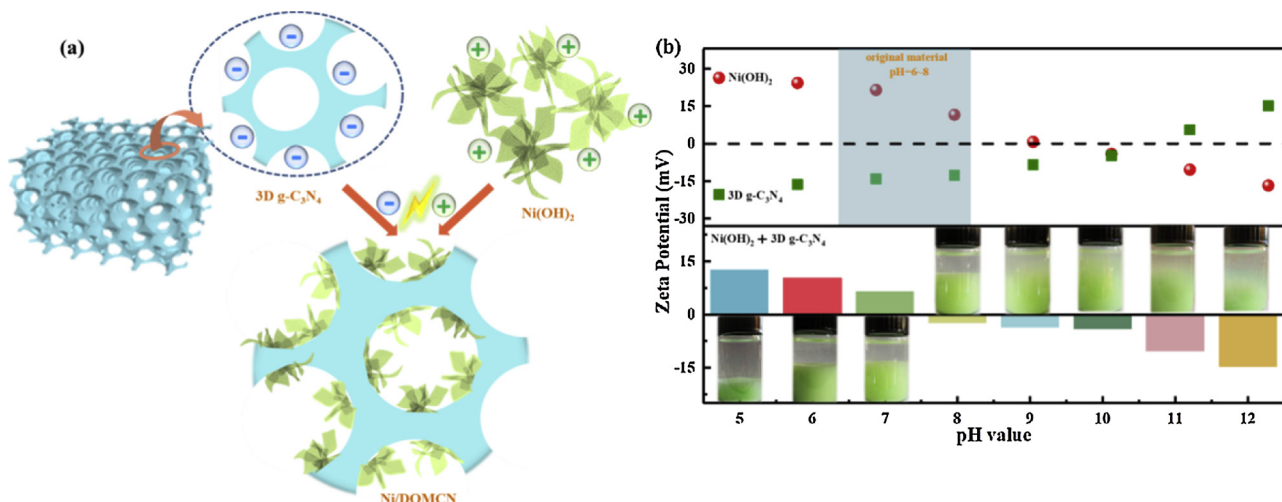


Fig. 1. (a) The schematic diagram of Ni/DOMCN photocatalyst constructed by electrostatic self-assembly using 3D $\text{g-C}_3\text{N}_4$ and Ni(OH)_2 nanosheets; (b) Zeta potential (mV) and photograph (inset) of a mixture of 3D $\text{g-C}_3\text{N}_4$ and Ni(OH)_2 at different pH values.

at different pH values, in which the precipitation rate of the material is significantly different in the range of pH \sim 5–12 within the same static time, attributing to the different potentials in different pH values [30].

The XRD patterns of pure 3D $\text{g-C}_3\text{N}_4$, pure Ni(OH)_2 , Ni/DOMCN are shown in Fig. 2 (a). Two peaks at \sim 13.0° and \sim 27.3° are observed in

pristine 3D $\text{g-C}_3\text{N}_4$, which are ascribed to the (100) and (002) crystal plane of 3D $\text{g-C}_3\text{N}_4$ corresponding to the repetitive in-plane tri-s-triazine units [31]. Diffraction peaks at \sim 34° or \sim 60.2° corresponding to Ni(OH)_2 are observed and pronouncedly strengthened within the Ni/DOMCN with the loading increase of the Ni(OH)_2 , indicating the

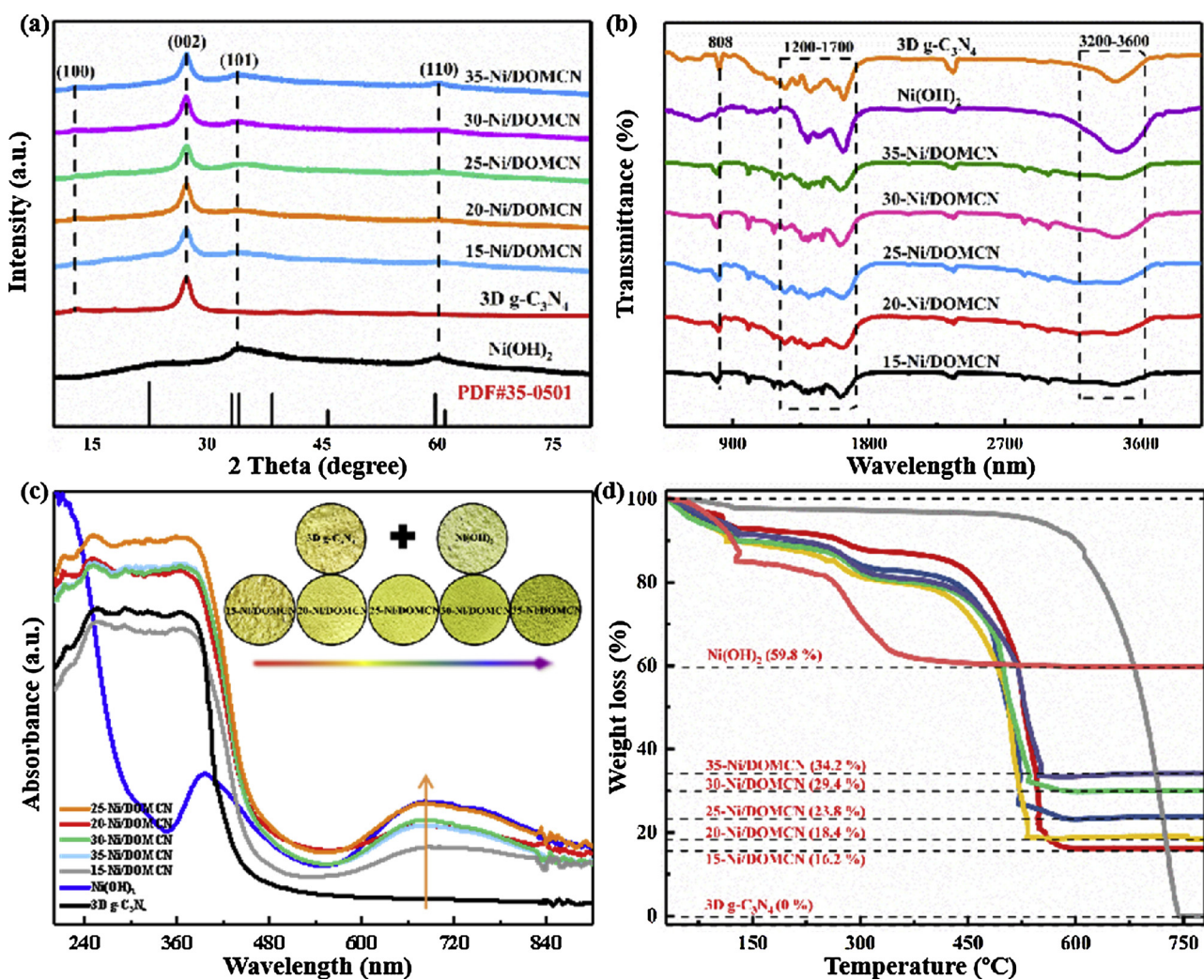
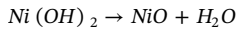


Fig. 2. XRD patterns (a), FT-IR spectra (b) UV-vis (c) and TG (d) of pure 3D $\text{g-C}_3\text{N}_4$, pure Ni(OH)_2 and Ni/DOMCN samples with different Ni(OH)_2 loading amount.

successful assembly of Ni(OH)_2 on 3D $\text{g-C}_3\text{N}_4$ with the electrostatic adsorption method. The FT-IR spectra in Fig. 2(b) exhibit the absorption peak at $\sim 808 \text{ cm}^{-1}$, which is due to the plane bending vibration of the tris-s-triazine unit of 3D $\text{g-C}_3\text{N}_4$. The broadband between ~ 1200 – 1700 cm^{-1} is owing to the typical CN and C=N stretching vibrations of the tris-s-triazine ring, and the absorption band during the scope of ~ 3200 – 3600 cm^{-1} is attributed to the tensile vibration of O–H [32]. Four infrared peaks at ~ 653 , ~ 973 , ~ 1080 and $\sim 3665 \text{ cm}^{-1}$ belong to Ni(OH)_2 [33]. Besides, the strength of the $\sim 1080 \text{ cm}^{-1}$ IR peak belonging to the O–H bending mode is enhanced with the increase of Ni(OH)_2 content. All the apparent characteristic FT-IR peaks of 3D $\text{g-C}_3\text{N}_4$ and Ni(OH)_2 are clearly observed, indicating their well-retained structures of 3D $\text{g-C}_3\text{N}_4$ and Ni(OH)_2 . UV–vis spectra in Fig. 2(c) show that the absorption edges of 2D/3D $\text{Ni(OH)}_2/\text{g-C}_3\text{N}_4$ architectures exhibit an apparent red shift compared with 3D $\text{g-C}_3\text{N}_4$, which will increase the absorption range of light, and improve photocatalytic activity as the full use of visible light. As the increment of Ni(OH)_2 loading, the absorption intensities of Ni/DOMCN in the visible range increase gradually, which are consistent with the color changes from yellow to blue, indicating the successful incorporation of Ni(OH)_2 . Further increasing Ni(OH)_2 weakens the light absorption intensity, caused by the "shading effect" of excessive Ni(OH)_2 . As the excessive Ni(OH)_2 nanosheets shield the pores of 3D $\text{g-C}_3\text{N}_4$ and also will act as recombination center of photogenerated electrons and holes, which is not conducive to light propagation and absorption.

The UV–vis spectra of Ni(OH)_2 show two absorption edge regions in the range of ~ 200 – 800 nm (~ 200 – 550 nm , ~ 550 – 800 nm). Among them, the wide absorption band from ~ 200 – 550 nm is due to the charge deliver from 2p oxygen to 3d orbital Ni^{2+} ions [34]. The enhanced absorption intensity at ~ 550 – 800 nm is induced by the charge transfer: the transitions of the electrons from the CB of 3D $\text{g-C}_3\text{N}_4$ to Ni^{2+} and the absorption of metallic Ni formed. This transfer of charges between the interfaces induces light trapping, producing more photoinduced electron-hole pairs for better photocatalytic activity [35,36]. The loading amount of Ni(OH)_2 in Ni/DOMCN was measured with TG curves and shown in Fig. 2(d). Three processes can be divided for the TG curves. A weight loss among the scope of ~ 30 – 130°C is due to the loss of water within the material, and the weight loss in ~ 130 – 300°C is caused by the transformation of Ni(OH)_2 into NiO . The conversion of $\text{g-C}_3\text{N}_4$ to carbon oxide and nitrogen oxide also induces the weight loss when the temperature is in the range of 300 – 780°C . When Ni(OH)_2 is heated, the generated H_2O is released from the material, and NiO is left after the heat treatment [25]:



The content of Ni(OH)_2 can be determined by calculating the content of NiO using the following formula (1) (2):

$$M_{\text{NiO}} = \frac{m^* \text{weight loss rate}}{M_{\text{NiO}}} \quad (1)$$

M_{NiO} : molar mass of NiO , M_{NiO} : relative molecular mass of NiO , m : overall mass of the composite. Since the molar mass of the NiO is consistent with the molar mass of the Ni(OH)_2 , the content of $M_{\text{Ni(OH)}_2}$ can be obtained from the weight loss of the composites:

$$\text{The content of } M_{\text{Ni(OH)}_2} = \frac{M_{\text{NiO}} * M_{\text{NiO}}}{m} * 100\% \quad (2)$$

After calculation, the loading of Ni(OH)_2 in 15-Ni/DOMCN, 20-Ni/DOMCN, 25-Ni/DOMCN, 30-Ni/DOMCN and 35-Ni/DOMCN nanocomposites are 19 wt.%, 22 wt.%, 30 wt.%, 36 wt.% and 42 wt.%, respectively. The optimum Ni(OH)_2 loading is 30 wt.%.

The N_2 adsorption and desorption isotherms as well as the relevant pore size distribution plots of the pure 3D $\text{g-C}_3\text{N}_4$, Ni(OH)_2 and 25-Ni/DOMCN samples are presented in Fig. 3(a–c). The corresponding plots for the 3D $\text{g-C}_3\text{N}_4$ materials with 15, 20, 30 and 35 ml Ni(OH)_2 are depicted in the Supporting Information (Fig. S1). The type IV nitrogen

adsorption–desorption isotherm indicate the formation of mesopores and macropores [37]. The surface area of 25-Ni/DOMCN ($76 \text{ m}^2/\text{g}$) is much higher than that of 3D $\text{g-C}_3\text{N}_4$ ($20 \text{ m}^2/\text{g}$), which owe to the attachment of Ni(OH)_2 nanosheets on the surfaces of 3D $\text{g-C}_3\text{N}_4$ pores, increasing the contact areas with the outside, and thereby the reactive sites and the hydrogen production efficiency. The photograph inserted in Fig. 3(d) illustrates that the volume of the Ni/DOMCN composites raises gradually along with the increase of Ni(OH)_2 loading, which will make the 3D $\text{g-C}_3\text{N}_4$ material more fluffy and larger specific surface areas owing to the loading of the Ni(OH)_2 nanosheets. However, the hydrogen production effect is gradually reduced with the increase of Ni(OH)_2 loading. We think that the excessive Ni(OH) loading blocks the 3D $\text{g-C}_3\text{N}_4$ channel, reducing the light reflection and the separation of electrons and holes [38]. The photocurrent curves (Fig. 8) also exhibit the higher recombination probability of electron-holes in 35-Ni/DOMCN, indicating that the surface area is not the only factor to affect hydrogen evolution.

The initially prepared silica nanospheres have a uniform diameter of about 400 nm (Fig. 4(a)), and a porous framework precursor of 3D $\text{g-C}_3\text{N}_4$ can be obtained after the removal of the SiO_2 nanospheres (Fig. 4(b–d)). These uniform nanopores are interconnected throughout 3D $\text{g-C}_3\text{N}_4$, which is beneficial to increase the active sites on the surfaces of the material as well as the transfer of species during the catalytic procedure. The 2D Ni(OH)_2 nanosheets are demonstrated in Fig. S2 and an ultra-thin transparent nanosheets structure is observed by the magnified TEM images (Fig. S2 (a–c)), which could provide abundant surface reaction sites and reduce the photogenerated charge diffusion length, and thus enhancing the photogenerated charge separation. The HRTEM image further confirmed the crystallinity of Ni(OH)_2 . The distance of $\sim 0.23 \text{ nm}$ corresponds to the (101) crystal plane in the Ni(OH)_2 lattice (Fig. S2 (d)). However, it is not able to clearly observe the Ni(OH)_2 nanosheets by SEM due to the small size (Fig. S2 (e, f)). Obviously, the ultra-thin nanosheet structures accelerate the diffusion of photogenerated carriers to the surface, thereby heighten their photocatalytic activity. It can be seen from Fig. 4(e–h) that the Ni(OH)_2 nanosheets are uniformly attached on the surfaces of 3D $\text{g-C}_3\text{N}_4$. Compared to 35-Ni/DOMCN (Fig. 4(g, h)), the Ni(OH)_2 nanosheets in the 25-Ni/DOMCN are attached more evenly and tightly to the surfaces of 3D $\text{g-C}_3\text{N}_4$ (Fig. 4(e, f)). The crystallinity of the two components and the heterojunction interface between the interfaces can be identified from HRTEM (Fig. 4(i)) and SAED pattern (Fig. 4(j)). In Fig. 4(i), the region I are assigned to amorphous 3D $\text{g-C}_3\text{N}_4$ catalyst. The lattice fringe spacing of 0.23 nm in region III are assigned to the (101) planes of Ni(OH)_2 , in good consistence with those of the (101) planes of standard Ni(OH)_2 (JCPDS PDF# 35-0501), which can be further validated by the SAED pattern with an obvious diffraction rings assigned to the (101) crystal planes. Region II, which is between regions I and III, can be considered the hetero-interface between $\text{g-C}_3\text{N}_4$ and Ni(OH)_2 .

The elemental mapping of the 25-Ni/DOMCN (Fig. 4(k, l)) displays homogeneous distribution of O, C, N and Ni across the selected area, which also shows the close contact of 2D Ni(OH)_2 to 3D $\text{g-C}_3\text{N}_4$. It can effectively facilitate the separation of photogenerated electrons and holes, promoting the transmission of electrons from 3D $\text{g-C}_3\text{N}_4$ to 2D Ni(OH)_2 , and improving photocatalytic activity, which can be further illustrated by the I–t, EIS and PL results.

The chemical composition of the sample is identified by XPS analysis and elucidating the interaction between the 2D Ni(OH)_2 and 3D $\text{g-C}_3\text{N}_4$. It can be seen from Fig. 5(a) that all the elements (including C, N, O and Ni) are detected in the measured spectra of Ni/DOMCN, indicating that the Ni/DOMCN photocatalyst has been successfully synthesized. In Fig. 5(b), the peaks at ~ 856.48 and $\sim 861.78 \text{ eV}$ accord to $\text{Ni} 2p^{3/2}$ and the peaks at ~ 874.18 and $\sim 880.4 \text{ eV}$ correspond to $\text{Ni} 2p^{1/2}$. The peaks for 25-Ni/DOMCN shift 2.1, 2.3, 2.4 and 2.4 eV towards higher binding energy than Ni(OH)_2 , respectively. In Fig. 5(c), the O 1s region can be deconvoluted into three peaks. Wherein, one peak at $\sim 529.8 \text{ eV}$ is ascribed to Ni-O-H in Ni(OH)_2 , and other peaks at

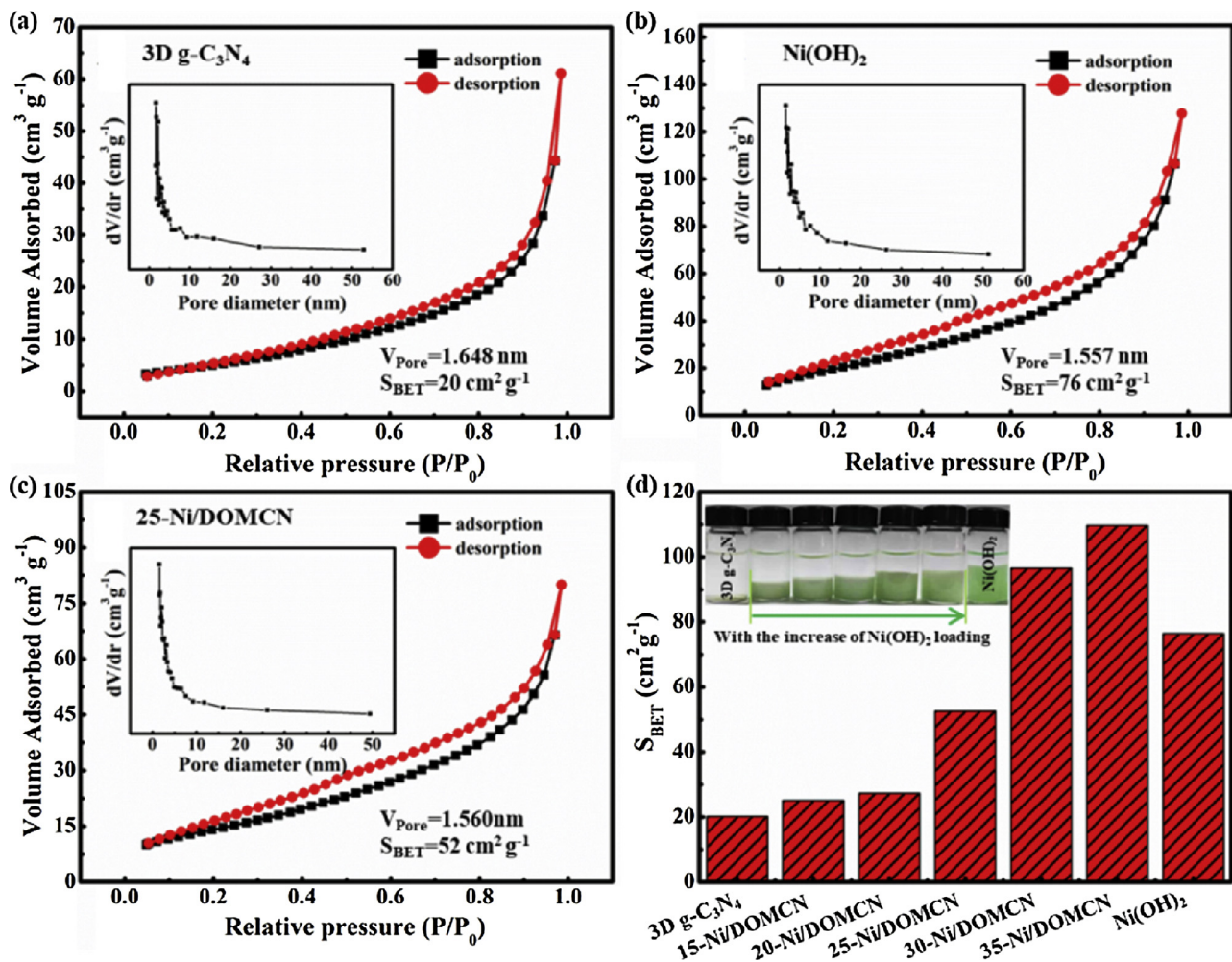


Fig. 3. N₂ adsorption-desorption analyses of (a) 3D g-C₃N₄, (b) Ni(OH)₂, (c) 25-Ni/DOMCN and (d) BET surface areas of all samples (photograph is shown in (d)). Insets (a, c) show the corresponding pore size distribution profiles.

~531.08 eV and ~532.08 eV correspond to C=O and O—H, respectively. Nevertheless, the peaks shift 1, 1.4 and 1.6 eV towards higher binding energy in O 1s spectrum of 25-Ni/DOMCN. Fig. 5(d) presents the corresponding high-resolution C 1s spectrum of 3D g-C₃N₄ and 25-Ni/DOMCN. The C 1s spectrum can be deconvoluted into two peaks at ~284.68 and ~288.18 eV. The peak at ~284.68 eV can be allocated to the C—C coordination of the surface amorphous carbon, and the peak (~288.18 eV) is attributed to the C-(N)₃ group [39]. Compared to that of 3D g-C₃N₄, the peaks of C 1s in 25-Ni/DOMCN transfer to lower binding energy. For the N 1s of 3D g-C₃N₄ in Fig. 5(e), the peaks at ~399.08 eV and ~400.98 eV are attributed to the tertiary nitrogen N(C)₃ and C-N-H groups, respectively. The N 1s peaks in 25-Ni/DOMCN are shifted to lower binding energies by 0.2 and 0.3 eV, respectively. After forming the Ni/DOMCN composite, the Ni 2p and O 1s peaks move to high energy, and the C 1s and N 1s peaks move toward low energy. The shift of these characteristic peaks indicates that 2D Ni(OH)₂ and 3D g-C₃N₄ not only form Ni/DOMCN composites by simple physical adsorption, but there is strong interaction and electron transfer between the two. It is further proved that a Z-scheme heterostructure is formed between Ni(OH)₂ and g-C₃N₄, which plays an important role in enhancing photocatalytic hydrogen evolution activity.

3.2. Photocatalytic H₂ evolution performances

The H₂ evolution activities of Ni/DOMCN photocatalyst with different Ni(OH)₂ loading after irradiation for 4 h under visible light

($\lambda > 400 \text{ nm}$) are shown in Fig. 6(a). The results show that Ni/DOMCN composites modified by Ni(OH)₂ photocatalyst exhibit improved photocatalytic H₂ evolution compared with unmodified 3D g-C₃N₄ (~4.59 μmol). It is proved that the formation of a Z-scheme heterojunction by coupling with a Ni(OH)₂ promotes the separation of photogenerated charges and enhances the evolutionary activity of H₂.

As shown in Fig. 6(c), the H₂ evolution rates of the samples first increase and then decrease with the increase of Ni(OH)₂ loading, and the maximum H₂ evolution rate of ~87.2 $\mu\text{mol h}^{-1}$ is realized for 25-Ni/DOMCN (~76 times higher than the unmodified 3D g-C₃N₄). While the photocatalytic activity decreases with the further increases of Ni(OH)₂ loading. We think that the excessive Ni(OH)₂ loading blocks the pores of 3D g-C₃N₄, reduces the incident light and acts as a recombination center for electron holes, thereby photocatalytic hydrogen evolution is reduced, which can be verified by TEM, I-t and EIS results (Fig. 4 and 8). It can be concluded that only proper loading amount of Ni(OH)₂ on the surface of 3D g-C₃N₄ can play role in improving photocatalytic activity. The AQE was studied by changing filters (365–520 nm) with different wavelengths under the same status (Fig. 6(b)) [19,40], and the calculated quantum efficiency is approximately 8.2% in the wavelength of 400 nm as shown in Fig. 6(d), which is well matched with light absorption curves, indicating that the evolution of H₂ is related to light induction. The stability of the 25-Ni/DOMCN photocatalyst was evaluated as shown in Fig. 6(e, f), it can be seen that ~1100 μmol H₂ after continuous irradiation for 12 h and the hydrogen evolution rate of the Ni/DOMCN composite remain at about ~315 μmol after 8 cycles,

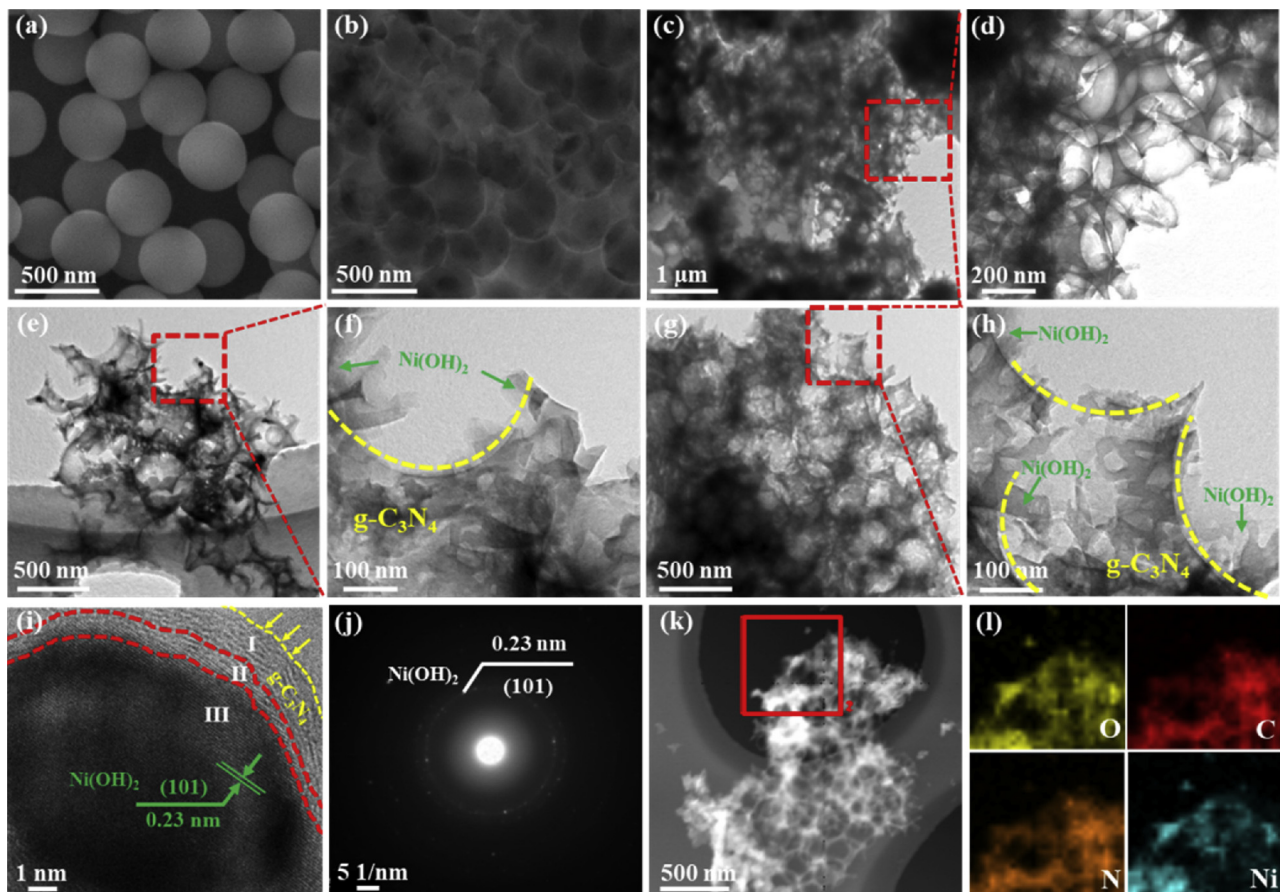


Fig. 4. SEM micrographs of (a) SiO_2 and (b) 3D $\text{g-C}_3\text{N}_4$; TEM of (c–d) 3D $\text{g-C}_3\text{N}_4$, (e, f) 25-Ni/DOMCN and (g, h) 35-Ni/DOMCN; (i) HRTEM image, (j) SAED pattern and (k, l) STEM images of the 25-Ni/DOMCN.

indicating good hydrogen evolution stability of the multi-component photocatalytic system of 3D/2D structures. Meantime, we further proved the cyclic stability of the 25-Ni/DOMCN catalyst after 8 cycles by TEM, XPS and XRD characterization. The 25-Ni/DOMCN catalyst after 8 cycles still has a clearly visible three-dimensional structure (Fig. S3 (a)). And in the partial enlargement (Fig. S3(b)), we can see that the 25-Ni/DOMCN catalyst has a slight flaking and the surface becomes rougher, but there are still visible three-dimensional aperture. It was proved that the structure of the 25-Ni/DOMCN catalyst did not receive serious damage after 8 cycles. As shown in Fig. S4 (a), The Ni 2p peaks in 25-Ni/DOMCN are shifted to lower binding energy after photocatalytic reaction, indicating that electron transfer occurs during the photocatalytic reaction. The weaker peak at 852.78 eV indicates the presence of Ni^0 . One possible explanation is that the photogenerated electrons in the CB of 3D $\text{g-C}_3\text{N}_4$ are transferred to Ni(OH)_2 , and these Ni^{2+} portions in Ni(OH)_2 are partially reduced to Ni^0 atoms to form Ni atoms. In addition to the diffraction peak of Ni(OH)_2 (Fig. S4 (b)), we can see that the 25-Ni/DOMCN composites exhibited a diffraction peak at 37.2° , 43.28° , 62.88° and 75.4° , which was attributed to the (111), (200), (220) and (311) diffraction planes of NiO (JCPDS, No. 47-1049), indicating that the presence of NiO nanocrystals in the 25-Ni/DOMCN nanocomposites. The reason is that the Ni atoms generated during the reaction are unstable in the air and are easily oxidized to form NiO . Therefore, we can concluded that the reasons of high cycling stability of the 25-Ni/DOMCN catalyst can be attributed as follows: (1) the superiority of the 2D/3D structure, wherein the 2D Ni(OH)_2 nanosheets are supported on the inner wall of 3D $\text{g-C}_3\text{N}_4$ to prevent aggregation and collapse; (2) The electrons reduce the free Ni^{2+} in aqueous solution to Ni^0 during the reaction. The Ni^0 are unstable in air, which can be easily oxidized to be NiO . The redox process between $\text{Ni}^{2+}/\text{Ni}^0/\text{NiO}$

makes Ni/DOMCN photocatalyst possess high cycle stability and promote the production of H_2 .

The superiority of 2D/3D Ni/DOMCN photocatalyst in photocatalytic H_2 production is further confirmed by control tests as shown in Fig. 7. $\text{g-C}_3\text{N}_4$ nanosheets (CNNS) and bulk $\text{g-C}_3\text{N}_4$ as substrates to grow Ni(OH)_2 nanosheets (NiNS) are used to demonstrate the effect of different morphologies of $\text{g-C}_3\text{N}_4$ on hydrogen production performance. In Fig. 7(a), the hydrogen production performance of Ni/DOMCN is 1.9 and 89 times higher than those of CNNS and untreated bulk $\text{g-C}_3\text{N}_4$, because the higher specific surface areas and more reactive sites of 2D/3D structural materials increase the reflection and utilization of light. To certificate the effect of NiNS in the hydrogen production process, Ni(OH)_2 with different morphologies are loaded on the 3D $\text{g-C}_3\text{N}_4$ substrates, such as Ni(OH)_2 nanoparticles (NiNP) and Ni(OH)_2 nanorods (NiNR). The results in Fig. 7(b) show that the hydrogen production effects of the NiNS are 1.8 and 1.6 times larger than those of NiNP and NiNR, respectively. We think the NiNS filled inside the 3D $\text{g-C}_3\text{N}_4$ not only provide a high specific surface area but also prevent the collapse of the 3D structure. At the same time, the ultra-thin NiNS structure can facilitate the swift transfer of electrons to the surface of the material to participate in the reaction. Furthermore, Ni(OH)_2 , which is a non-precious metal catalysts, has a lower cost and a broader application prospect compared with precious metal catalysts. Three precious metal co-catalysts such as $\text{MoS}_2/\text{DOMCN}$, Pt/DOMCN and Au/DOMCN are prepared to compare the performance of photocatalytic hydrogen evolution as shown in Fig. 7(c), the hydrogen evolution performance of the non-precious metal catalyst Ni(OH)_2 is higher than that other precious metal co-catalysts as the photocatalytic activity of the sample not only depends on the noble metal ions but also depends on the crystal structure and crystallinity, etc. Modification of 3D $\text{g-C}_3\text{N}_4$ material by

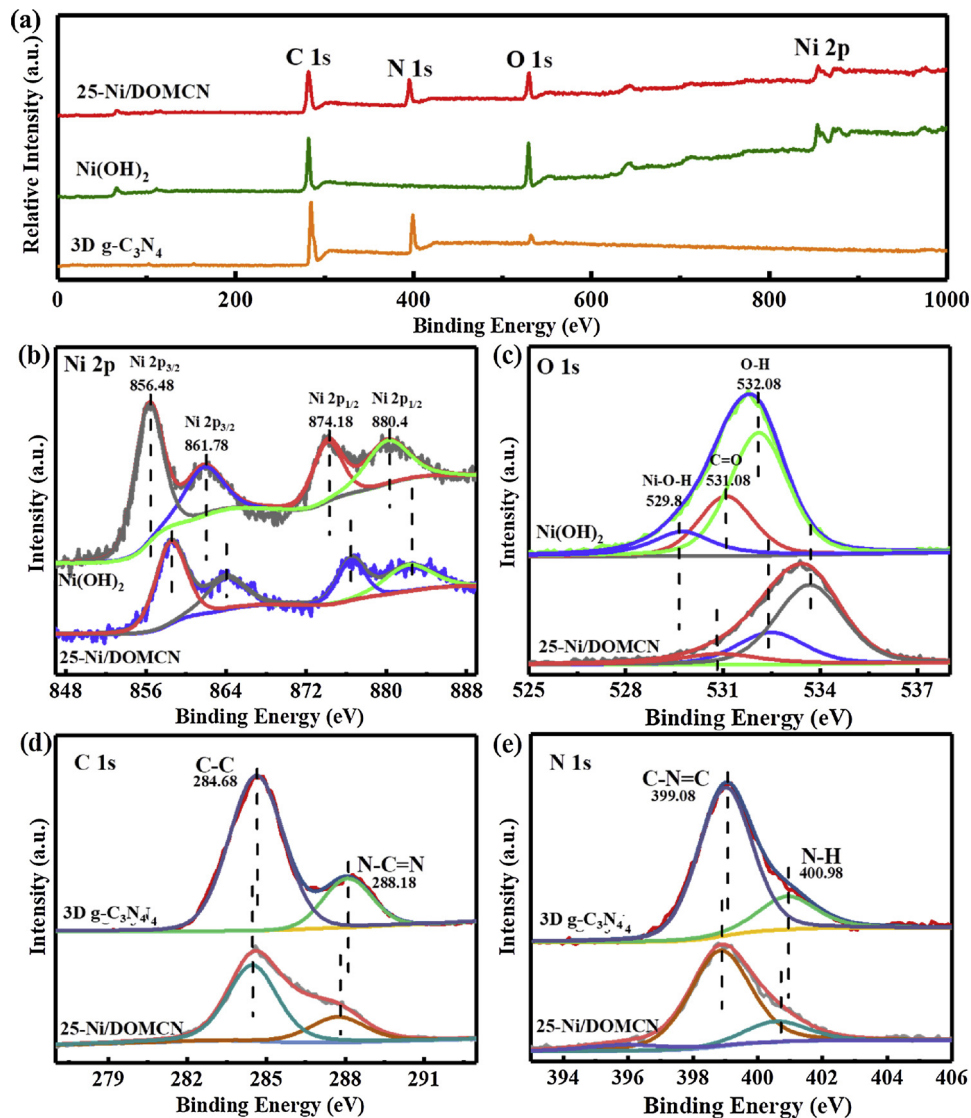


Fig. 5. XPS spectra of (a) survey for 3D $\text{g-C}_3\text{N}_4$, Ni(OH)_2 and 25-Ni/DOMCN; (b) Ni 2p and (c) O 1s in Ni(OH)_2 and 25-Ni/DOMCN; (d) C 1s and (e) N 1s in $\text{g-C}_3\text{N}_4$ and 25-Ni/DOMCN.

crystallized 2D Ni(OH)_2 catalyst can provide more active sites for H_2 precipitation and facilitate the separation and migration of photo-generated charge carriers. The photocatalytic H_2 production activities of different Ni specie-containing photocatalysts (including NiO , NiS and NiP) in Fig. 7(d) indicate that the Ni/DOMCN modified by NiNS shows the best activity compared to other Ni species modification, which is 2.5, 1.8 and 1.3 times to those of NiO , NiS and NiP , respectively. The efficiency of NiNS for photocatalytic hydrogen evolution is attributed to the following two aspects: (1) the ultra-thin NiNS are more conducive to electron migration to the surface; (2) the Ni(OH)_2 has a large solubility product constant, which can release more free Ni^{2+} and obtain Ni^0 by photoreduction, then the Ni^0 is oxidized to NiO . The redox reaction between $\text{Ni}^{2+}/\text{Ni}^0/\text{NiO}$ can promote the photocatalytic reaction.

The PL spectra in Fig. 8(a) show that the PL emission intensity of Ni/DOMCN composites significantly reduced compared with pure 2D $\text{g-C}_3\text{N}_4$, indicating that the introduction of Ni(OH)_2 nanosheets promotes electron transfer and reduces photogenerated electrons-empty recombination of the pair [41]. As the 2D Ni(OH)_2 loading increases, the intensities of PL emissions firstly decrease and then increase, and the 25-Ni/DOMCN catalyst shows the lowest PL emission intensity, which is consistent with its photocatalytic hydrogen evolution performance. In addition, time-resolved PL is used to study the charge life (Fig. 8(b)).

The exponential decay function is fitted by the following equation (B_1 , B_2 are the pre-function and τ_1 , τ_2 are the corresponding lifetimes, respectively):

Where the average life expectancy τ is estimated by the following equation:

$$\tau = \frac{B_1 \tau_1^2 + B_2 \tau_2^2}{B_1 \tau_1 + B_2 \tau_2}$$

The τ of 25-Ni/DOMCN (~0.98 ns) is significantly higher than pure 3D $\text{g-C}_3\text{N}_4$ (~2.05 ns) and Ni(OH)_2 (~1.67 ns), demonstrated that coupling the Ni(OH)_2 catalyst to 3D $\text{g-C}_3\text{N}_4$ significantly increased the separation of photogenerated charges and raise the charge life. In other words, the electrons can be rapidly transferred from 3D $\text{g-C}_3\text{N}_4$ to the Ni(OH)_2 material and shorten the electron transport time. The charge separation efficiency and mobility of the photocatalyst are investigated using an I-t curve under periodic irradiation for 10 s. As shown in Fig. 8(c), the 3D $\text{g-C}_3\text{N}_4$ shows lower photocurrent intensity under the potential of 0.7 V vs. Ag/AgCl , while the photocurrent responses for the 25-Ni/DOMCN composite is prompt, steady and reproducible, demonstrating that the modification of Ni(OH)_2 increases the separation and transmit efficiency of electron-hole pairs [42]. However, the photocurrent responses are clearly decreased for 35-Ni/DOMCN because of

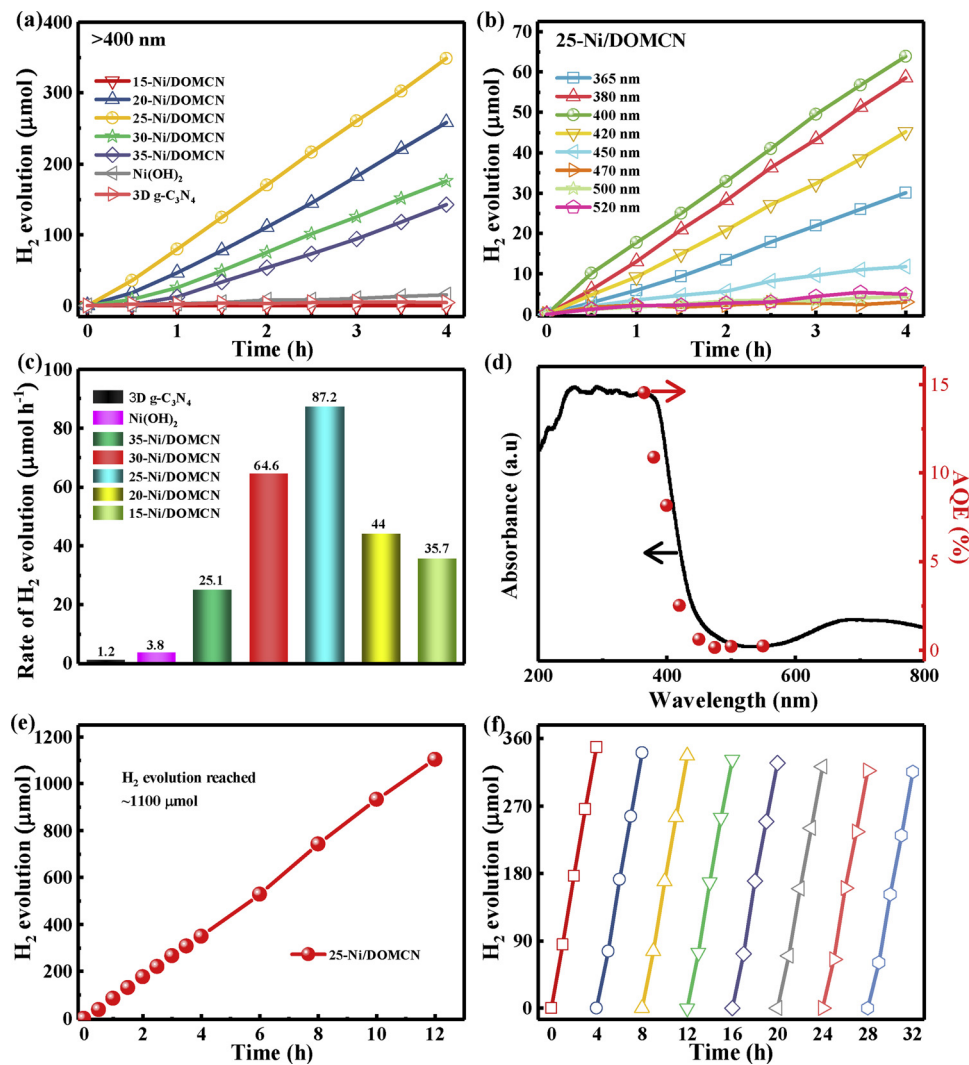


Fig. 6. (a) Photocatalytic H₂ evolution performances of different photocatalysts; (b) 25-Ni/DOMCN photocatalysts hydrogen production efficiency in different spectra; (c) Photocatalytic H₂ evolution rate of different photocatalysts; (d) Wavelength dependent H₂ evolution rate and UV-vis DRS spectra of 25-Ni/DOMCN; (e) Photocatalytic stability and (f) Cycling test of photocatalytic H₂ evolution of 25-Ni/DOMCN.

the excessive Ni(OH)₂ loading, which blocks the contact between Ni(OH)₂ and 3D g-C₃N₄ and reduces the separation of photogenerated charges. The EIS Nyquist plots in Fig. 8(d) show the smallest semicircle of 25-Ni/DOMCN, indicating its small charge-migrating resistance. The charge transfer resistance of 35-Ni/DOMCN is larger than 25-Ni/DOMCN, which is matched with previous TEM results, BET data and hydrogen production effects. The EIS Nyquist plots were modeled with equivalent circuit (inset in Fig. 8(d)) using Z-view software, and R_s is the solution resistance; R_{ct} is the electron-transfer resistance [7]. The excessive specific surface area will produce more surface defects, which become the recombination center of electron holes, resulting in a decrease in the number of carriers. Therefore, only a proper amount of Ni(OH)₂ can be used to effectively promote the separation and transfer of photogenerated charges at the catalyst interface. A comparison table of the hydrogen evolution of the photocatalyst containing g-C₃N₄ is given, which proves that the 3D/2D Ni/DOMCN photocatalyst exhibits excellent photocatalytic performance (Table. S1).

The band structures of 3D g-C₃N₄ and Ni(OH)₂ were studied to understand the effects of Ni(OH)₂ loading on the photogenerated e⁻-h⁺ separation, migration and transfer among the photocatalytic process [43]. The band gap value of 3D g-C₃N₄ and Ni(OH)₂ that estimated by a related curve of $(\alpha h\nu)^{1/2}$ vs. hν, which was shown in Fig. S5 (a). The band gaps of 3D g-C₃N₄ and Ni(OH)₂ were estimated to be 3.0 eV and

3.15 eV, respectively. According to the VB XPS spectrum (Fig. S5 (b)), the VB position of 3D g-C₃N₄ and Ni(OH)₂ is determined to be +1.68 eV and -0.12 eV. Then the CB edge position of 3D g-C₃N₄ and Ni(OH)₂ were determined to be -1.32 eV and -3.27 eV according to the formula: E_{CB} = E_{VB} - E_g.

We compared the wavelength-dependent H₂ evolution rate and UV-vis DRS spectra of pure 3D g-C₃N₄ and 25-Ni/DOMCN. The H₂ signal could not be detected at monochromatic illumination of 550, 600, 650 and 700 nm, which is related to the absorption edge of 3D g-C₃N₄ (Fig. S6 (a)). The 25-Ni/DOMCN composites with Ni(OH)₂-loaded can detect progressively enhanced H₂ signals at 550, 600, 650 and 700 nm monochromatic illumination in Fig. S6 (b), which can be attributed to Ni(OH)₂ spectral absorption [44]. It can be seen from the absorption spectrum of Ni(OH)₂ that there is a large absorption peak at around $\lambda > 550$ nm. The progressively enhanced H₂ signal in the 25-Ni/DOMCN is derived from the absorption of the spectrum by the Ni(OH)₂ nanomaterials. The results showed that the improvement of hydrogen evolution performance of 25-Ni/DOMCN is derived from the heterostructure between Ni(OH)₂ and 3D g-C₃N₄.

To investigate whether the electron transfer mechanism of 25-Ni/DOMCN material belongs to the conventional type-II or the Z-scheme, we have further conducted the measurements of HRTEM (Fig. 9) and surface photovoltage spectroscopy (SPS, Fig. 10) [45,46]. The

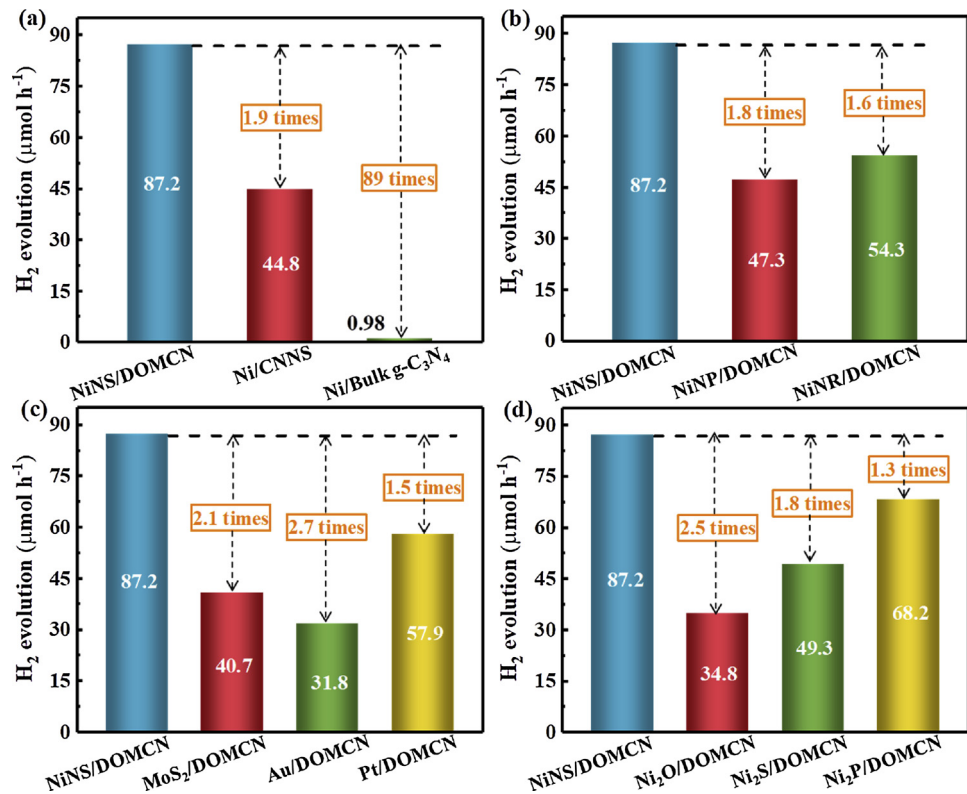


Fig. 7. Comparison of the photocatalytic hydrogen evolution rate of the Ni/DOMCN samples with (a) different g-C₃N₄ substrates; (b) different shapes of Ni(OH)₂; (c) different precious metals; (d) different compounds of Ni.

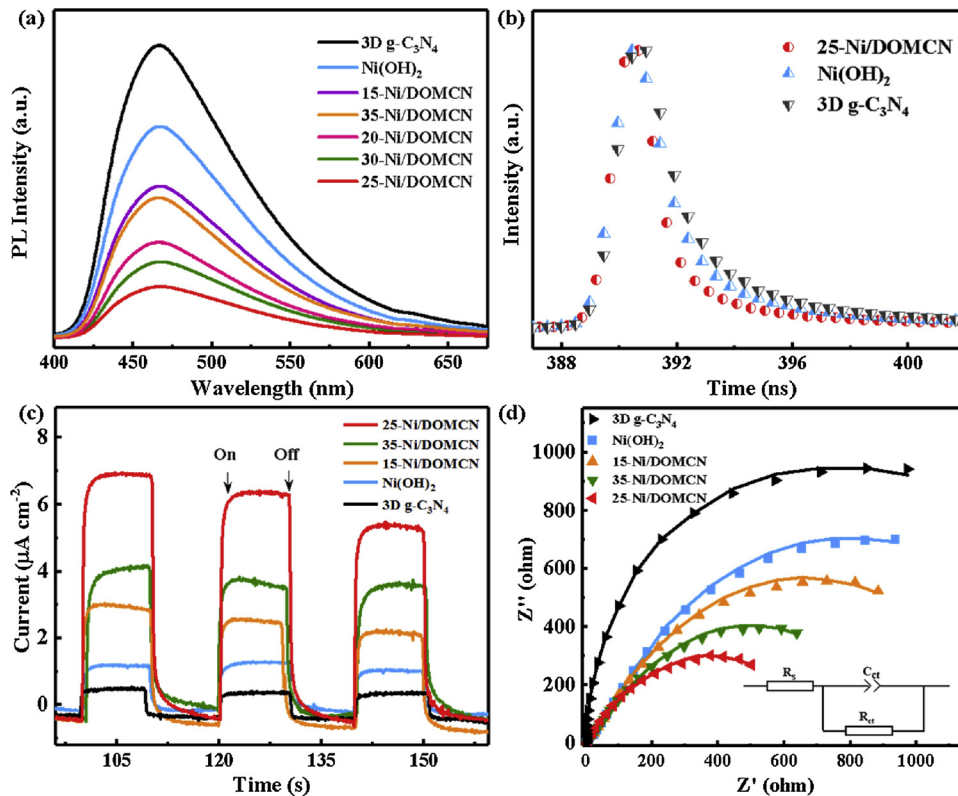


Fig. 8. (a) Photoluminescence spectra, (c) I-t responses and (d) EIS Nyquist plots and (The solid line was fitted by Z-view software using the proposed equivalent circuit model, the inset shows an ideal equivalent circuit for the working photoelectrode) of pure 3D g-C₃N₄, Ni(OH)₂ and Ni/DOMCN catalysts; fluorescence decay curves (b) of pure 3D g-C₃N₄, Ni(OH)₂ and 25-Ni/DOMCN catalysts samples.

photodeposition of Pt and PbO₂ nanoparticle was also carried out for 25-Ni/DOMCN. Generally, Pt⁴⁺ in H₂PtCl₆ can be reduced to Pt⁰ in the form of Pt nanoparticles by the photoinduced electrons. Therefore, as obtained Pt nanoparticles tend to accumulate around electron-rich sites.

Pb(NO₃)₂ can be characterized by the oxidation of holes to PbO₂, which can characterize the transport path of holes. As shown in Fig. 9(a, b), there are two different lattice fringes on the surface of the amorphous 3D g-C₃N₄, in which the distance of ~0.23 nm corresponds to the (101)

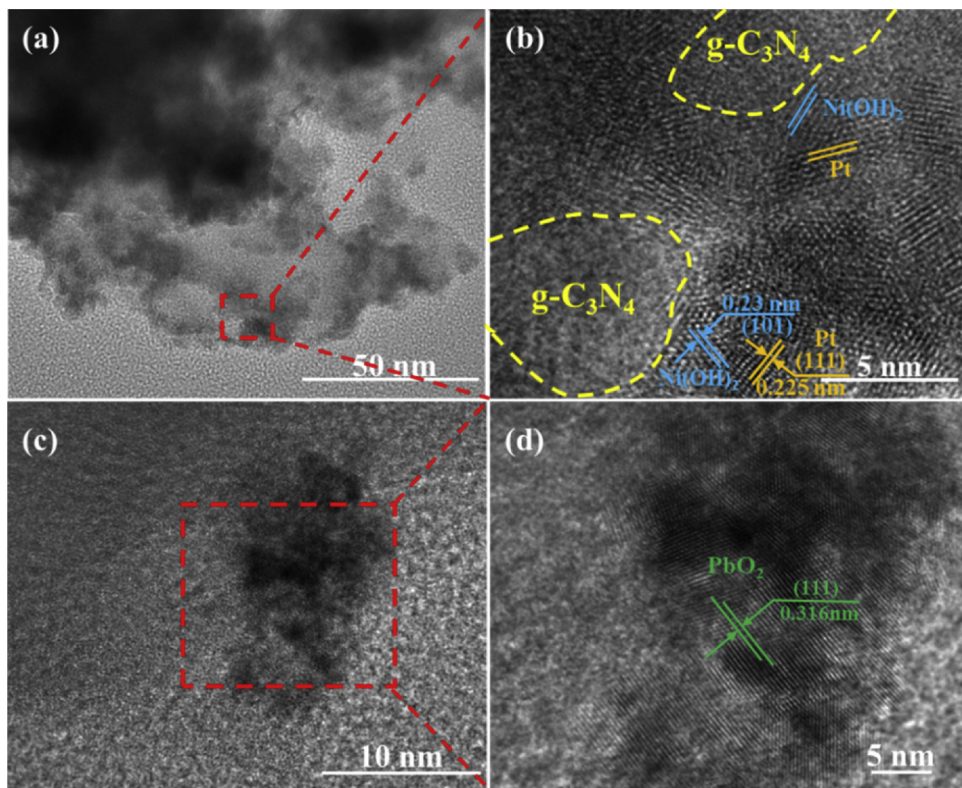


Fig. 9. HRTEM images of 25-Ni/DOMCN photodeposited with Pt (a, b) nanoparticles and PbO₂ nanoparticles (c, d).

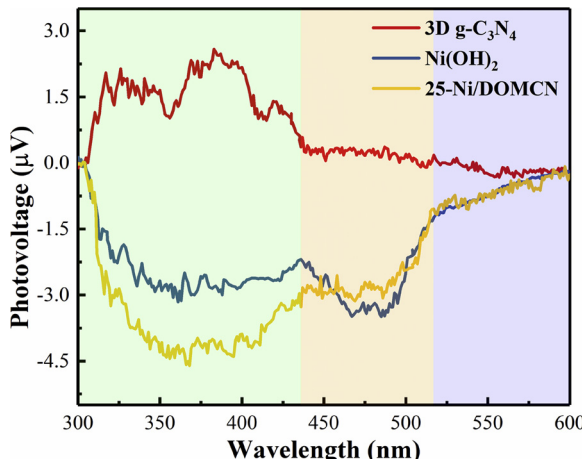


Fig. 10. SPS of 3D g-C₃N₄, Ni(OH)₂ and 25-Ni/DOMCN. The signal intensity of 25-Ni/DOMCN was divided by 300 to fit into the plot.

crystal plane in the Ni(OH)₂ lattice and the lattice fringe spacing of 0.225 nm can be ascribed to Pt nanoparticles existed on the Ni(OH)₂ surface. This implies that the Pt nanoparticles are gathered on/around Ni(OH)₂ rather than randomly dispersed on the 3D g-C₃N₄, demonstrating that photoinduced electrons in the CB of Ni(OH)₂ remain on the original site as predicted by the Z-scheme route instead of transferring to the CB of 3D g-C₃N₄ through the conventional type-II mechanism. Furthermore, the lattice edge space of 0.316 nm in Fig. 9(c, d) corresponds to (111) plane of PbO₂, indicating that the PbO₂ nanoparticles are directly deposited onto the surface of 3D g-C₃N₄. It proves that the holes don't metastasize and still locate in the VB of 3D g-C₃N₄, which is consistent with the charge transfer mechanism of the Z-scheme heterojunction. These charge tracking results manifest the formation of Z-scheme type for 25-Ni/DOMCN instead of the conventional type-II photocatalyst.

To further investigate the charge transfer route, the SPS of 25-Ni/DOMCN was investigated in comparison with those of 3D g-C₃N₄ and Ni(OH)₂. In Fig. 10, it shows an obvious positive photovoltage response in the range of 300–440 nm for 3D g-C₃N₄, which is the typical feature of an n-type semiconductor [47,48]. In contrast, Ni(OH)₂ shows a negative SPS response. Furthermore, the SPS signal of the 25-Ni/DOMCN composite is negative, similar to that of Ni(OH)₂, herein, the formation of the type Z-scheme heterojunction is further confirmed. As shown in Fig. 10, a weaker SPS signal is observed in the long wavelength region because only Ni(OH)₂ absorbs light from this region and the light absorption performance is low. The light absorption increases with the wavelength shortened, the formation of the Z-scheme material causes more electrons to remain in Ni(OH)₂, and the SPS signal becomes more negative, similar to the case of pure Ni(OH)₂, which means that the electrons stay on the Ni(OH)₂ and follow the behavior of it. Based on the above results of SRS and TEM, we can conclude that 25-Ni/DOMCN is a Z-scheme type instead of the conventional type-II photocatalyst.

The Z-scheme heterojunction was proposed in Fig. 11. Under light irradiation, the photogenerated electrons on the CB of 3D g-C₃N₄ will transfer to the VB of Ni(OH)₂ and combine with holes there. In this way, photogenerated carriers' separation can be enhanced, resulting in improved photocatalytic activity as compared with Ni(OH)₂ and 3D g-C₃N₄. The stronger reductive electrons are left on the CB of Ni(OH)₂ to participate in H₂ evolution process, and leaving the stronger oxidizing holes on the VB of 3D g-C₃N₄ to participate in the oxidation reaction of sacrificial agent triethanolamine [49]. In addition to the promotion of charge separation by Z-scheme system, the hollow structure of the 3D g-C₃N₄ and the sheet structure of Ni(OH)₂ may also benefit the photocatalytic process. The special structure of 2D/3D provides more surface active sites, and the hollow structure promotes multiple reflections of light [50]. In summary, the Ni/DOMCN material with 2D/3D structure is beneficial to the improvement of the photocatalytic performance.

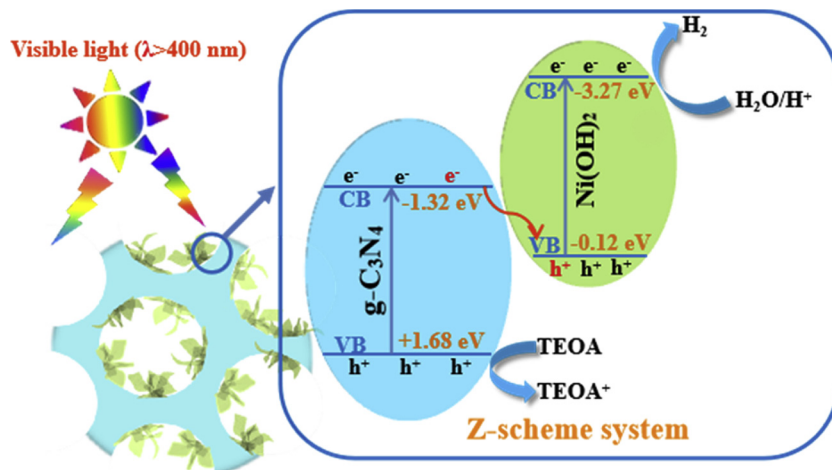


Fig. 11. Schematic illustration of Ni/DOMCN for photocatalytic H_2 evolution.

4. Conclusion

In conclusion, non-precious metal 2D/3D Ni/DOMCN heterojunctions based on Z-scheme system of electron transportation was successfully self-assembled by an electrostatic method. As a low-cost, stable and efficient photocatalyst, whose hydrogen production performance can be regulated by loading amount of $Ni(OH)_2$. The H_2 evolution rate of the 3D $g\text{-}C_3N_4$ photocatalyst supported by $Ni(OH)_2$ promoter (30 wt.%) is the highest ($\sim 87.2 \mu\text{mol h}^{-1}$), which is ~ 76 times higher than that of pure 3D $g\text{-}C_3N_4$. The significant improvement in photocatalytic performance can be ascribed to the excellent surface contact of $Ni(OH)_2$ nanosheets with 3D $g\text{-}C_3N_4$, which promote visible light absorption and improved efficiency of electron transfer and charge separation. In addition, the synthesized 2D/3D Ni/DOMCN prove to have a comparative highly cycle stability. The present work is anticipated to provide novel insights for rational design of 2D/3D structures and the preparation of Z-catalyst catalysts.

Declaration of Competing Interest

The authors declare that they have no known competing financial interests or personal relationships that could have appeared to influence the work reported in this paper.

Acknowledgements

The work was financially by the National Natural Science Foundation of China (Grant Nos. 51672109, 21505050, 21707043), Natural Science Foundation of Shandong Province for Excellent Young Scholars (ZR2016JL015), Natural Science Foundation of Shandong Province (Grant No. ZR2017BEE005).

Appendix A. Supplementary data

Supplementary material related to this article can be found, in the online version, at doi:<https://doi.org/10.1016/j.apcatb.2019.117997>.

References

- [1] J. Sun, M. Ren, L. Yu, Z. Yang, L. Xie, F. Tian, Y. Yu, Z. Ren, S. Chen, H. Zhou, Highly efficient hydrogen evolution from a mesoporous hybrid of nickel phosphide nanoparticles anchored on cobalt phosphosulfide/phosphide nanosheet arrays, *Small* 15 (2019) 1804272.
- [2] B. Sun, W. Zhou, H. Li, L. Ren, P. Qiao, W. Li, G. Fu, Synthesis of particulate hierarchical tandem heterojunctions toward optimized photocatalytic hydrogen production, *Adv. Mater.* 25 (2018) 1804282.
- [3] G. Zhao, Y. Sun, W. Zhou, X. Wang, K. Chang, G. Liu, H. Liu, T. Kako, J. Ye, Superior photocatalytic H_2 production with cocatalytic Co/Ni species anchored on sulfide semiconductor, *Adv. Mater.* 25 (2017) 1703258.
- [4] C. Sun, H. Zhang, H. Liu, X. Zheng, W. Zou, L. Dong, L. Qi, Enhanced activity of visible-light photocatalytic H_2 evolution of sulfur-doped $g\text{-}C_3N_4$ photocatalyst via nanoparticle metal Ni as cocatalyst, *Appl. Catal. B: Environ.* 235 (2018) 66.
- [5] C. Li, S. Yu, H. Che, X. Zhang, J. Han, Y. Mao, Y. Wang, C. Liu, H. Dong, Fabrication of Z-scheme heterojunction by anchoring mesoporous $\gamma\text{-}Fe_2O_3$ nanospheres on $g\text{-}C_3N_4$ for degrading tetracycline hydrochloride in water, *ACS Sustain. Chem. Eng.* 6 (2018) 16437.
- [6] D. Ruan, S. Kim, M. Fujitsuka, T. Majima, Defects rich $g\text{-}C_3N_4$ with mesoporous structure for efficient photocatalytic H_2 production under visible light irradiation, *Appl. Catal. B: Environ.* 238 (2018) 638–646.
- [7] H. Gao, H. Yang, J. Xu, S. Zhang, J. Li, Strongly coupled $g\text{-}C_3N_4$ nanosheets- Co_3O_4 quantum dots as 2D/0D heterostructure composite for peroxyomonosulfate activation, *Small* 2 (2018) 1801353.
- [8] H. Gao, R. Cao, S. Zhang, H. Yang, X. Xu, Three-dimensional hierarchical $g\text{-}C_3N_4$ architectures assembled by ultrathin self-doped nanosheets: extremely facile hexamethylenetetramine activation and superior photocatalytic hydrogen evolution, *ACS Appl. Mater. Inter.* 11 (2019) 2050.
- [9] N. Tian, Y. Zhang, X. Li, K. Xiao, X. Du, F. Dong, G. Waterhouse, T. Zhang, H. Huang, Precursor-reforming protocol to 3D mesoporous $g\text{-}C_3N_4$ established by ultrathin self-doped nanosheets for superior hydrogen evolution, *Nano Energy* 38 (2017) 72.
- [10] S. Zhang, H. Gao, Y. Huang, X. Wang, T. Hayat, J. Li, X. Xu, X. Wang, Ultrathin $g\text{-}C_3N_4$ nanosheets coupled with amorphous Cu-doped FeOOH nanoclusters as 2D/0D heterogeneous catalysts for water remediation, *Environ. Sci.: Nano* 5 (2018) 1179.
- [11] Z. He, J. Fu, B. Cheng, J. Yu, S. Cao, $Cu_2(OH)_2CO_3$ clusters: novel noble-metal-free cocatalysts for efficient photocatalytic hydrogen production from water splitting, *Appl. Catal. B: Environ.* 205 (2017) 104.
- [12] H. Gao, R. Cao, X. Xu, S. Zhang, Y. Huang, H. Yang, X. Deng, J. Li, Construction of dual defect mediated Z-scheme photocatalysts for enhanced photocatalytic hydrogen evolution, *Appl. Catal. B: Environ.* 245 (2019) 399.
- [13] R. Cao, H. Yang, X. Deng, S. Zhang, X. Xu, In-situ synthesis of amorphous silver silicate/carbonate composites for selective visible-light photocatalytic decomposition, *Sci. Rep.* 7 (2017) 15001.
- [14] M. Zalfani, B. Schueren, Z. Hu, J. Rooke, R. Bourguiga, M. Wu, Y. Li, G. Tendeloo, B. Su, Novel 3DOM $BiVO_4/TiO_2$ nanocomposites for highly enhanced photocatalytic activity, *J. Mater. Chem. A* 3 (2015) 21244.
- [15] B. Lin, J. Li, B. Xu, X. Yan, B. Yang, J. Wei, G. Yang, Spatial positioning effect of dual cocatalysts accelerating charge transfer in three dimensionally ordered macroporous $g\text{-}C_3N_4$ for photocatalytic hydrogen evolution, *Appl. Catal. B: Environ.* 243 (2019) 94–105.
- [16] S. Sun, S. Liang, Recent advances in functional mesoporous graphitic carbon nitride ($mpg\text{-}C_3N_4$) polymers, *Nanoscale* 9 (2017) 10544.
- [17] R. Cao, H. Yang, X. Deng, P. Sun, S. Zhang, X. Xu, Construction of 3DOM carbon nitrides with quasi-honeycomb structures for efficient photocatalytic H_2 production, *ChemCatChem* 10 (2018) 5656–5664.
- [18] S. Sun, Y. Zhang, G. Shen, Y. Wang, X. Liu, Z. Duan, L. Pan, X. Zhang, J. Zou, Photoinduced composite of Pt decorated $Ni(OH)_2$ as strongly synergistic cocatalyst to boost H_2O activation for photocatalytic overall water splitting, *Appl. Catal. B: Environ.* 243 (2019) 253–261.
- [19] J. Liu, Q. Jia, J. Long, X. Wang, Z. Gao, Q. Gu, Amorphous NiO as co-catalyst for enhanced visible-light-driven hydrogen generation over $g\text{-}C_3N_4$ photocatalyst, *Appl. Catal. B: Environ.* 222 (2018) 35–43.
- [20] J. Fu, Q. Xu, J. Low, C. Jiang, J. Yu, Ultrathin 2D/2D $WO_3/g\text{-}C_3N_4$ step-scheme H_2 -production photocatalyst, *Appl. Catal. B: Environ.* 243 (2019) 556.
- [21] Q. Ma, X. Peng, M. Zhu, X. Wang, Y. Wang, H. Wang, Strategic modulation of electron migration in the $TiO_2\text{-}Au\text{-}Cds$: Z-scheme design for the enhancement in hydrogen evolution reaction, *Electrochim. Commun.* 95 (2018) 28–32.
- [22] L. Zhang, W. Feng, B. Wang, K. Wang, F. Gao, Y. Zhao, P. Liu, Construction of dual-channel for optimizing Z-scheme photocatalytic system, *Appl. Catal. B: Environ.* 1

212 (2017) 80–88.

[23] R. Bhosale, S. Jain, C. Vinod, S. Kumar, S. Ogale, Direct Z-scheme g-C₃N₄/FeWO₄ nanocomposite for enhanced and selective photocatalytic CO₂ reduction under visible light, *ACS Appl. Mater. Inter.* 11 (2019) 6174–6183.

[24] W. Huang, X. Ma, H. Wang, R. Feng, J. Zhou, P. Duchesne, P. Zhang, F. Chen, N. Han, F. Zhao, J. Zhou, W. Cai, Y. Li, Promoting effect of Ni(OH)₂ on palladium nanocrystals leads to greatly improved operation durability for electrocatalytic ethanol oxidation in alkaline solution, *Adv. Mater.* 4 (2017) 1703057.

[25] A. Meng, S. Wu, B. Cheng, J. Yu, Xu J, Hierarchical TiO₂/Ni(OH)₂ composite fibers with enhanced photocatalytic CO₂ reduction performance, *J. Mater. Chem. A* 6 (2018) 4729.

[26] X. Li, H. Zhang, J. Luo, Z. Feng, J. Huang, Hydrothermal synthesized novel nanoporous g-C₃N₄/MnTiO₃ heterojunction with direct Z-scheme mechanism, *Electrochim. Acta* 258 (2017) 998–1007.

[27] N. Nie, L. Zhang, J. Fu, B. Cheng, J. Yu, Self-assembled hierarchical direct Z-scheme g-C₃N₄/ZnO microspheres with enhanced photocatalytic CO₂ reduction performance, *Appl. Surf. Sci.* 441 (2018) 12–22.

[28] S. Liu, J. Zhou, H. Song, 2D Zn-hexamine coordination frameworks and their derived N-rich porous carbon nanosheets for ultrafast sodium storage, *Adv. Energy Mater.* 6 (2018) 1800569.

[29] J. Fu, C. Bie, B. Cheng, C. Jiang, J. Yu, Hollow CoS_x polyhedrons act as high-efficiency cocatalyst for enhancing the photocatalytic hydrogen generation of g-C₃N₄, *ACS Sustain. Chem. Eng.* 6 (2018) 2767.

[30] X. Dong, Cheng F, Recent development in exfoliated two-dimensional g-C₃N₄ nanosheets for photocatalytic application, *J. Mater. Chem. A* 3 (2015) 23642.

[31] J. Wang, Z. Yang, X. Gao, W. Yao, W. Wei, X. Chen, R. Zong, Y. Zhu, Core-shell g-C₃N₄@ZnO composites as photoanodes with double synergistic effects for enhanced visible-light photoelectrocatalytic activities, *Appl. Catal. B: Environ.* 217 (2017) 169.

[32] Y. Tan, Z. Shu, J. Zhou, T. Li, W. Wang, Z. Zhao, One-step synthesis of nanosstructured g-C₃N₄/TiO₂ composite for highly enhanced visible-light photocatalytic H₂ evolution, *Appl. Catal. B: Environ.* 230 (2018) 260.

[33] Q. Xu, H. Jiang, H. Zhang, Y. Hu, C. Li, Heterogeneous interface engineered atomic configuration on ultrathin Ni(OH)₂/Ni₃S₂ nanoforests for efficient water splitting, *Appl. Catal. B: Environ.* 242 (2018) 60.

[34] R. Rather, S. Singh, B. Pal, A C₃N₄ surface passivated highly photoactive Au-TiO₂ tubular nanostructure for the efficient H₂ production from water under sunlight irradiation, *Appl. Catal. B: Environ.* 213 (2017) 9.

[35] Y. Wang, W. Yang, X. Chen, J. Wang, Y. Zhu, Photocatalytic activity enhancement of core-shell structure g-C₃N₄@TiO₂ via controlled ultrathin g-C₃N₄ layer, *Appl. Catal. B: Environ.* 220 (2018) 337.

[36] C. Yang, J. Qin, Z. Xue, M. Ma, X. Zhang, R. Liu, Rational design of carbon-doped TiO₂ modified g-C₃N₄ via in-situ heat treatment for drastically improved photocatalytic hydrogen with excellent photostability, *Nano Energy* 41 (2017) 1.

[37] C. Wang, K. Guo, W. He, X. Deng, P. Hou, F. Zhuge, X. Xu, T. Zhai, Hierarchical CuCo₂S₄@NiMn-layered double hydroxide core-shell hybrid arrays as electrodes for supercapacitors, *Sci. Bull.* 62 (2017) 1122.

[38] C. Zhang, Y. Zhou, J. Bao, X. Sheng, J. Fang, S. Zhao, Y. Zhang, W. Chen, Hierarchical honeycomb Br, N-codoped TiO₂ with enhanced visible-light photocatalytic H₂ production, *ACS Appl. Mater. Inter.* 10 (2018) 18796.

[39] X. Qian, Y. Wu, M. Kan, M. Fang, D. Yue, J. Zeng, Y. Zhao, FeOOH quantum dots coupled g-C₃N₄ for visible light driving photo-fenton degradation of organic pollutants, *Appl. Catal. B: Environ.* 237 (2018) 513.

[40] G. Zhao, G. Liu, H. Pang, H. Liu, H. Zhang, K. Chang, X. Meng, X. Wang, J. Ye, Improved photocatalytic H₂ evolution over g-carbon nitride with enhanced in-plane ordering, *Small* 12 (2016) 6160.

[41] J. Wu, N. Li, X. Zhang, H. Fang, Y. Zheng, X. Tao, Heteroatoms binary-doped hierarchical porous g-C₃N₄ nanobelts for remarkably enhanced visible-light-driven hydrogen evolution, *Appl. Catal. B: Environ.* 226 (2017) 61.

[42] R. Wang, X. Kong, W. Zhang, W. Zhu, L. Huang, J. Wang, X. Zhang, X. Liu, N. Hu, Y. Suo, J. Wang, Mechanism insight into rapid photocatalytic disinfection of salmonella based on vanadate QDs-interspersed g-C₃N₄ heterostructures, *Appl. Catal. B: Environ.* 225 (2017) 228.

[43] K. He, J. Xie, X. Luo, J. Wen, S. Ma, X. Li, Y. Fang, X. Zhang, Enhanced visible light photocatalytic H₂ production over Z-scheme g-C₃N₄ nanosheets/WO₃ nanorods nanocomposites loaded with Ni(OH)_x cocatalysts, *Chinese J. Catal.* 38 (2017) 240–252.

[44] J. Ran, J. Yu, M. Jaroniec, Rational design and electron transfer kinetics of MoS₂/CdS nanodotson-nanorods for efficient visible-light-driven hydrogen generation, *Green Chem.* 13 (2011) 2708.

[45] P. Tan, Y. Liu, A. Zhu, W. Zeng, H. Cui, J. Pan, Rational design of z-scheme system based on 3D hierarchical CdS supported 0D Co₉S₈ nanoparticles for superior photocatalytic H₂ generation, *ACS Sustainable Chem. Eng.* 6 (2018) 10385–10397.

[46] Q. Li, T. Shi, X. Li, K. Lv, M. Li, F. Liu, H. Li, M. Lei, Remarkable positive effect of Cd (OH)₂ on CdS semiconductor for visible-light photocatalytic H₂ production, *Appl. Catal. B: Environ.* 229 (2018) 8–14.

[47] W. Jiang, X. Zong, L. An, S. Hua, X. Miao, S. Luan, Y. Wen, F. Tao, Z. Sun, Consciously constructing heterojunction or direct Z-Scheme photocatalysts by regulating electron direction, *ACS Catal.* 8 (2018) 2209–2217.

[48] L. Jing, X. Sun, J. Shang, W. Cai, Z. Xu, Y. Du, H. Fu, Review of surface photovoltage spectra of nanosized semiconductor and its applications in heterogeneous photocatalysis, *Sol. Energ. Mat. Sol. C* 79 (2003) 133–151.

[49] W. Wang, T. An, G. Li, D. Xia, H. Zhao, J. Yu, P. Wong, Earth-abundant Ni₂P/g-C₃N₄ lamellar nanohydrids for enhanced photocatalytic hydrogen evolution and bacterial inactivation under visible light irradiation, *Appl. Catal. B: Environ.* 217 (2017) 570–580.

[50] M. Altomare, N. Nguyen, S. Hejazi, P. Schmuki, A cocatalytic electron-transfer cascade site-selectively placed on TiO₂ nanotubes yields enhanced photocatalytic H₂ evolution, *Adv. Funct. Mater.* 28 (2017) 1704259.